THE JOURNAL OF BIOLOGICAL CHEMISTRY VOL. 285, NO. 53, pp. 41982–41992, December 31, 2010

Identification of a Residue in Helix 2 of Rice Plasma Membrane Intrinsic Proteins That Influences Water Permeability*[S]

Received for publication, January 11, 2010, and in revised form, September 29, 2010 Published, JBC Papers in Press, October 6, 2010, DOI 10.1074/jbc.M110.101790

Minhua Zhang[‡1,2], Shouqin Lü[§¶1], Guowei Li[‡3], Zhilei Mao[‡], Xin Yu[‡4], Weining Sun[‡], Zhangcheng Tang[‡], Mian Long[§¶5], and Weiai Su[‡6]

From the [‡]Institute of Plant Physiology and Ecology, Shanghai Institutes for Biological Sciences, Chinese Academy of Sciences, Shanghai 200032 and the [§]Key Laboratory of Microgravity (National Microgravity Laboratory) and [¶]Center for Biomechanics and Bioengineering, Institute of Mechanics, Chinese Academy of Sciences, Beijing 100190, China

Molecular selection, ion exclusion, and water permeation are well known regulatory mechanisms in aquaporin. Water permeability was found to be diverse in different subgroups of plasma membrane intrinsic proteins (PIPs), even though the residues surrounding the water holes remained the same across the subgroups. Upon homology modeling and structural comparison, a conserved Ala/Ile(Val) residue difference was identified in helix 2 that affected the conformation of the NPA region and consequently influenced the water permeability. The residue difference was found to be conservative within the two subgroups of PIPs in rice as well as in other plants. Functional tests further confirmed the prediction via site-directed mutagenesis where replacement of Ala^{103} or Ala^{102} in respective OsPIP1;1 or OsPIP1;3 with Val yielded 7.0- and 2.2-fold increases in water transportation, and substitution of Ile^{98} or Val^{95} in respective OsPIP2;3 or OsPIP2;7 with Ala resulted in 73 or 52% reduction of water transportation. Based on structural analyses and molecular dynamics simulations, we proposed that the difference in water permeability was attributed to the orientation variations of helix 2 that modified water-water and water-protein interactions.

Aquaporins (AQPs)[7] are small integral membrane proteins that facilitate water transport across the membranes and are widely distributed in animals, plants, and microbes. It is unique in plants that AQPs form a large family with 35 and 33 members in *Arabidopsis* and rice, respectively. According to the amino acid sequence, the AQPs could be classified into four subgroups, *i.e.* the plasma membrane intrinsic proteins (PIPs), the tonoplast intrinsic proteins, the NOD26-like intrinsic protein, and the small basic intrinsic proteins (reviewed in Maurel *et al.* (1) and references cited therein). Plant PIPs are divided into two phylogenic subgroups, PIP1 and PIP2 (2). The AQP monomer consists of six transmembrane α-helices tilted along the plane of the membrane and connected by five loops (A–E). Loop B and D as well as the N and C termini are cytoplasmic (3). Two highly conserved constrictions within the pore of AQPs were proposed by structural analysis of AQP proteins. One is the central constriction formed by two Asn-Pro-Ala (NPA) motifs located on two short α-helices and the other is the outer constriction or aromatic/arginine (ar/R) constriction formed by spatial arrangement of four aromatic amino acids. Recently it was found that in addition to facilitating the transport of water, AQPs also can transport other small solutes. Size exclusion at the two main constrictions is one of the mechanisms for water transport and substrate selectivity by AQPs (3, 4). Extensive investigation of the plant PIPs revealed that PIP2 paralogues induced water permeation when expressing on *Xenopus* oocyte or yeast membranes, whereas PIP1 paralogues were almost inactive (5–10). The sequence difference between the two subgroups, however, is quite subtle, as they share the same residues in main pore constrictions and almost the same hydrophobic residues around the aqueous pathway (6, 11).

The first attempt to elucidate the mechanism of distinct water transport activities between the two subgroups was performed in radish PIPs (12). Based on the sequence difference, the authors identified a residue that discriminates PIP1s and PIP2s. They further showed that substitution of Ile^{244} (at the pore entrance) in RsPIP1–3 with Val enhanced the activity to 250% of WT. Replacement of Val^{235} with Ile (corresponding to Ile^{244} in RsPIP1–3) resulted in a remarkable activity reduction to 45% of WT RsPIP2-2. This work provided evidence that punctual structural differences between the two PIP subgroups can to some extent explain their distinct water transport activity.

Crystal structures of mammalian AQP1 (13, 14) and AQP0 (15–17), bacterial GlpF (4, 18) and AqpZ (19), archaeal AqpM (20), and plant SoPIP2 (21) have provided important informa-

* This work was supported by National Natural Science Foundation of China Grants 30670172, 30730032, and 10332060, National Key Basic Research Foundation of China Grant 2006CB910303, Knowledge Innovation Program of Chinese Academy of Science Grants KSCX2-YW-N-011 and KJCX2-YW-L08, and National High Technology Research and Development Program of China Grants 2007AA100603 and 2007AA02Z306.

[S] The on-line version of this article (available at http://www.jbc.org) contains supplemental Figs. S1–S5.

[1] Both authors contributed equally to this work.

[2] Present address: Cell Communication Lab, Division of Applied Life Science, Gyeongsang National University, 6-306, Gajwadong 900, Jinju 660-701, Korea.

[3] Present address: Biochimie et Physiologie Moléculaire des Plantes, SupAgro/INRA/CNRS/UM2 UMR 5004, 2, Place Viala, F-34 060 Montpellier Cedex, France.

[4] Present address: Institutes of Biology II, Faculty of Biology, Albert-Ludwigs-Universität of Freiburg, Schänzlestrasse 1, D-79104 Freiburg, Germany.

[5] To whom correspondence may be addressed: No. 15 North 4th Ring Rd., Beijing 100190, China. Tel.: 86-10-8254-4131; Fax: 86-10-8254-4131; E-mail: mlong@imech.ac.cn.

[6] To whom correspondence may be addressed: Fenglin Rd. 300, Shanghai 200032, China. Tel.: 86-21-54924245; Fax: 86-21-54924015; E-mail: zstressc@online.sh.cn.

[7] The abbreviations used are: AQP, aquaporin; PIP, plasma membrane intrinsic protein; MD, molecular dynamics.

tion related to water permeability (P_f). Combined with structure-function analyses and molecular dynamics (MD) simulations, these structures have provided detailed pictures for water transportation and gating mechanisms of AQPs. Specific features of pore radius, residue side chain orientation/fluctuation, and energy barrier were proposed to affect water transport. For example, a narrow constriction at the NPA region was found to be essential for AQP1 water selectivity and permeability (22). Point mutations in the ar/R region changed the substrate specificity of the AQP1 and allowed the mutant protein to permeate urea, glycerol, ammonia, and proton (23). AQP0 has a specific constriction near the cytoplasmic region in addition to those at the ar/R and NPA regions (15–17). The Tyr^{23} residue at the NPA region and the Tyr^{149} residue at the cytoplasmic constriction were shown to play important roles in restraining water permeation through AQP0 (24). The differences of the key residues at three constriction regions resulted in lower permeability of AQP0 than AQP1 (25). In addition, the side chain dynamics were found to be a prerequisite for water permeation in AQP1 (26). In fact, water permeation via AQPs appears to be a dynamic and statistical process, *i.e.* the instantaneous pore radius or energy barriers do not directly restrict bulk water motion. This may account for the apparent discrepancy between channel radius and P_f in typical AQPs (27). Osmotic permeability matrix analysis was proposed as a way to explain P_f with respect to structural characteristics, where the water channel was decomposed into small local regions, and the channel permeability contributed to those from the regions themselves (diagonal elements of P_f matrix) and those from the cross-correlation of different regions (off-diagonal elements of P_f matrix) (27). Comparisons of the P_f matrix of five aquaporins (AQP0, AQP1, AQP4, AqpZ, and GlpF) at the three constriction regions indicated that the NPA region hinders the collective motion of the water chain. The weakest correlation across the NPA region is observed in the P_f correlation matrix of AQP0, which indicated that water motion at one end of the channel does not propagate to the other end (27, 28). These reports prompt us to unravel the details of interactions of channel water-water and water-protein in the two plant PIP subclasses, because the former promotes water permeability and the latter has a contrary effect.

Here, we integrated structural comparison, functional measurements, and MD simulations to address this issue. We show that an Ala/Ile(Val) residue at the NPA region dominates the permeability difference between OsPIP1s and OsPIP2s. Our results indicate that this residue contributes to the different water transportation activities of the two subgroups via modulating the molecular conformation around both the NPA and the ar/R regions.

EXPERIMENTAL PROCEDURES

Homology Modeling of OsPIPs and Sequence Alignment of Plant PIPs—Target structure of each WT or mutated OsPIP protein was generated by GeneAltas software (Accelrys Inc.) (29) using the default setting. For each PIP protein, 2–3 structure models were generated by homology modeling, and only the one listed at rank 1 with the highest score was selected (Fig. 1) and used for further analysis. The algorithm PB90, the sequence profile-based searching protocol utilizing optimized PSI-BLAST, and the algorithm THM, the high throughput modeling protocol with subsequent verification with Profiles-3D and PMF Verify, were used by the software to select reference template from the template data base and to make the structure. The x-ray crystallography of bovine AQP1 (Protein Data Bank code 1J4N) was automatically selected as the best reference template (13) from three candidates (RCSB template 1J4N, 1H6I, and 1DLF). All the structures were visualized in VMD (30), and the channel radius of each protein was calculated using HOLE software (31). All PIPs were aligned using MUSCLE software (32), and the detailed sequence data source are listed in supplemental material.

Site-directed Mutagenesis of OsPIPs—Full-length cDNAs of OsPIP1;1, OsPIP1;3, OsPIP2;3, and OsPIP2;7 were obtained from rice mRNA using RT-PCR. PCR was used to perform all the site-directed mutagenesis aforementioned. Briefly, mutant primers were designed for each OsPIP protein as follows: forward, 5′-gca tga tct tcg tcc tcg tct act g-3′, and reverse, 5′-cag tag acg agg acg agg atc atg c-3′, for OsPIP1;1 A103V; forward, 5′-gca tga tct tcg tcc tcg tct act g-3′, and reverse, 5′-cag tag acg agg acg agg atc atg c-3′, for OsPIP1;3 A102V; forward, 5′-gca tga tct tcg cgc tcg tct act g-3′, and reverse, 5′-cag tag acg agc gcg aag atc atg c-3′, for OsPIP2;3 I98A; and forward, 5′-cca cca tat tcg ccc tcg tct act g-3′, and reverse, 5′-cag tag acg agg gcg aat atg gtg g-3′, for OsPIP2;7 V95A. The mutant primers were coupled with full-length primers to produce the mutant gene. The WT and mutated cDNAs of each OsPIP were cloned into the expression vector pXβG-ev1 at the BglII site and sequenced for accuracy.

Osmotic Permeation Assay— cRNA of the WT and mutant OsPIPs were produced by using mMESSAGE mMACHINE capped RNA transcription T3 kit (Ambion, Austin, TX). The cRNA was quantified by UV spectrum and stored as 1 μg/μl at −80 °C. *Xenopus laevis* oocytes were prepared and injected with cRNAs as described previously (33). Oocytes were injected with 23.5 nl of sterile water (control) or an equal volume of cRNA solution. Oocyte swelling was measured directly after transferring from 200 to 40 mosM ND96 solution as described previously (34). The section area (S) of oocytes was calculated using LabWorks3.0 (UVP, United Kingdom). Water permeability per cell was calculated by $P_f = V_0(d(V/V_0)/dt)/(S_0 \times V_w \times (\mathrm{OsM_{in}} - \mathrm{OsM_{out}}))$ where the initial oocyte volume, V_0, is 9×10^{-4} cm^3; the initial oocyte area, S_0, is 0.045 cm^2; and the molar volume of water, V_w, is 18 cm^3/mol (35). At least 20 oocytes were tested for each protein. The statistical significance of the difference in P_f between WT and mutated OsPIPs was assessed using Student's t test.

Membrane Expression of WT and Mutated OsPIPs in Xenopus Oocytes—For GFP-fused proteins, the cDNA fragments of WT and mutant OsPIPs without a stop codon were inserted between the EcoRI and XbaI site of expression vector pGEMHE pre-inserted with a GFP sequence. The cRNA of each GFP-fused protein was synthesized *in vitro* by mMESSAGE mMACHINE capped RNA transcription T7 kit (Ambion).

The fluorescence signal was visualized by laser confocal microscopy (Leica, Germany). Five oocytes were tested for each protein where cross-membrane fluorescence intensity for each cell was measured from eight positions along one-quarter of the membrane. The mean fluorescence intensity was then obtained by averaging the intensities from five cells in each case. The Student's *t* test was used to analyze statistical significance of the fluorescence intensity difference between WTs and correspondent mutants.

Molecular Dynamics Simulations of OsPIP1;1 and OsPIP2;7—All simulations for OsPIP1;1, OsPIP1;1 A103V, OsPIP2;7, and OsPIP2;7 V95A were carried out using the respective monomeric homology model generated using Protein Data Bank code 1J4N as template. Each system was composed of a channel tetramer, 1-palmitoyl-2-oleoyl-*sn*-glycero-3-phosphatidylethanolamine lipid bilayer, a 25-Å thick slab of water neutralized by 100 mM chloride and sodium ions. All simulations were performed using NAMD2 (36) and CHARMM27 force field (37) in periodic boundary conditions with time steps of 1 fs. A smooth (10–12 Å) cutoff and the Particle Mesh Ewald method were used to calculate van der Waals and electrostatic interactions. All simulations were done at constant temperature (300 K) and pressure (1 atm) and analyzed using the VMD program.

A collective diffusion model, proposed to characterize the osmotic permeability of a channel upon equilibrium MD simulations (38), was used here to evaluate water permeation of simulated OsPIP1;1, OsPIP2;7, and their respective mutants. Briefly, in Equation 1 the osmotic permeability P_f of the channel gives

$$P_f = v_w \times D_n \quad \text{(Eq. 1)}$$

where v_w is the average volume of a single water molecule, and D_n is defined as the diffusion coefficient of channel waters at equilibrium. By taking advantage of MD simulations that the movement of every water molecule is able to be monitored, a collective coordinate, *n*, is defined to quantify channel water translocation as shown in Equation 2,

$$dn = \sum_{i \in s(t)} dZ_i/L \quad \text{(Eq. 2)}$$

where *L* is the channel length along *Z* direction; $s(t)$ denotes the set of channel water molecules at time *t*, and dZ_i is the displacement of *i*th water molecule along *Z* direction at the interval d*t*. At equilibrium, the net amount of water permeation through the channel is zero on average, *i.e.* $\langle n(t) \rangle = 0$. Mean square displacement of *n*, $\langle n^2(t) \rangle$, obeys the Einstein relation when *t* is much longer than the velocity correlation time of *n* as shown in Equation 3,

$$\langle n^2(t) \rangle = 2D_n \times t \quad \text{(Eq. 3)}$$

Thus, one can determine P_f from Equation 1 using D_n value calculated from the collective coordinate *n* (Equations 2 and 3).

RESULTS

Identifying Important Residues for P_f Difference in Two OsPIP Subgroups—We generated three-dimensional structures of all OsPIPs using GeneAtlas and analyzed their pore radii by HOLE. Each OsPIP presented a narrow radius at the ar/R constriction region (Fig. 1, *red lines*). OsPIP1;1 and OsPIP1;3, but not OsPIP1;2, had an extra constriction at the NPA region with narrow pore radius. All the OsPIP2s, except OsPIP2;1 and OsPIP2;8, did not have such extra constriction at the NPA region (Fig. 1, *dark green lines*). Structural comparison of OsPIP1;1, OsPIP1;3, OsPIP2;3, and OsPIP2;7 at the NPA and ar/R constriction regions indicated that the orientation change of an Ile side chain at the NPA region might induce the difference in pore radius between the two subgroups because the hydrophobic $Ile^{101/100}$ side chains in OsPIP1;1/1;3 point to the pore, and the $Ile^{96/93}$ side chains in OsPIP2;3/2;7 orient away from the pore (Fig. 2*A*, *green licorice*). As a conservative pore-forming residue, the orientation change of Ile side chain at the NPA region could possibly induce the low (in OsPIP1) or high (in OsPIP2) water permeation efficiency across the membrane. To identify the key residues responsible for the orientation change, 15 neighboring residues around the Ile site were analyzed within the maximum distance (6 Å) of van der Waals force (Fig. 2*B*). Comparisons of the neighboring residues around the Ile^{101} of OsPIP1;1 and Ile^{93} of OsPIP2;7 revealed the discriminating residues between PIP1s and PIP2s that is Ala^{103} in OsPIP1;1 and Val^{95} in OsPIP2;7. The Ala residue presented in three PIP1s and the Ile residue in all the OsPIP2s except OsPIP2;7 and OsPIP2;8, which had a Val residue at the corresponding site (Fig. 2*B*). Therefore, the difference at the Ala/Ile(Val) site was conservative in OsPIP1s and OsPIP2s. This finding suggested that the conserved site might be a potential candidate to induce the diverse orientation of the Ile residue between the two OsPIPs, which in turn affected the P_f.

Structural Analyses of Ala/Ile(Val)-mutated OsPIPs—To test the hypothesis, the impact of the Ala/Ile(Val) site on side chain orientation of the Ile residue was analyzed by comparing the pore radii and structures of OsPIPs with their corresponding interchanged mutants. The virtual structures of four mutated OsPIPs, OsPIP1;1 A103V, OsPIP1;3 A102V, OsPIP2;3 I98A, and OsPIP2;7 V95A, were generated, and the corresponding pore radii were calculated. A nascent narrow NPA region was formed inside the pore of OsPIP2;3 I98A and OsPIP2;7 V95A mutant proteins (Fig. 3*A*, *dark green lines*), which was in accordance with the orientation change of Ile^{96} side chain in OsPIP2;3 I98A or Ile^{93} side chain in OsPIP2;7 V95A (Fig. 3*B*, *green licorice*), respectively. In addition, the pore radius at the ar/R region of OsPIP2;7 V95A was also getting bigger. By contrast, this constriction region became wider in OsPIP1;1 A103V, but no radius change was observed in OsPIP1;3 A102V (Fig. 3*A*, *dark green lines*), which was in agreement with the minor orientation change of Ile^{101} side chain in OsPIP1;1 A103V and the invisible change of the Ile^{100} side chain in OsPIP1;3 A102V (Fig. 3*B*, *green licorice*), respectively. In addition, an orientation change of the long

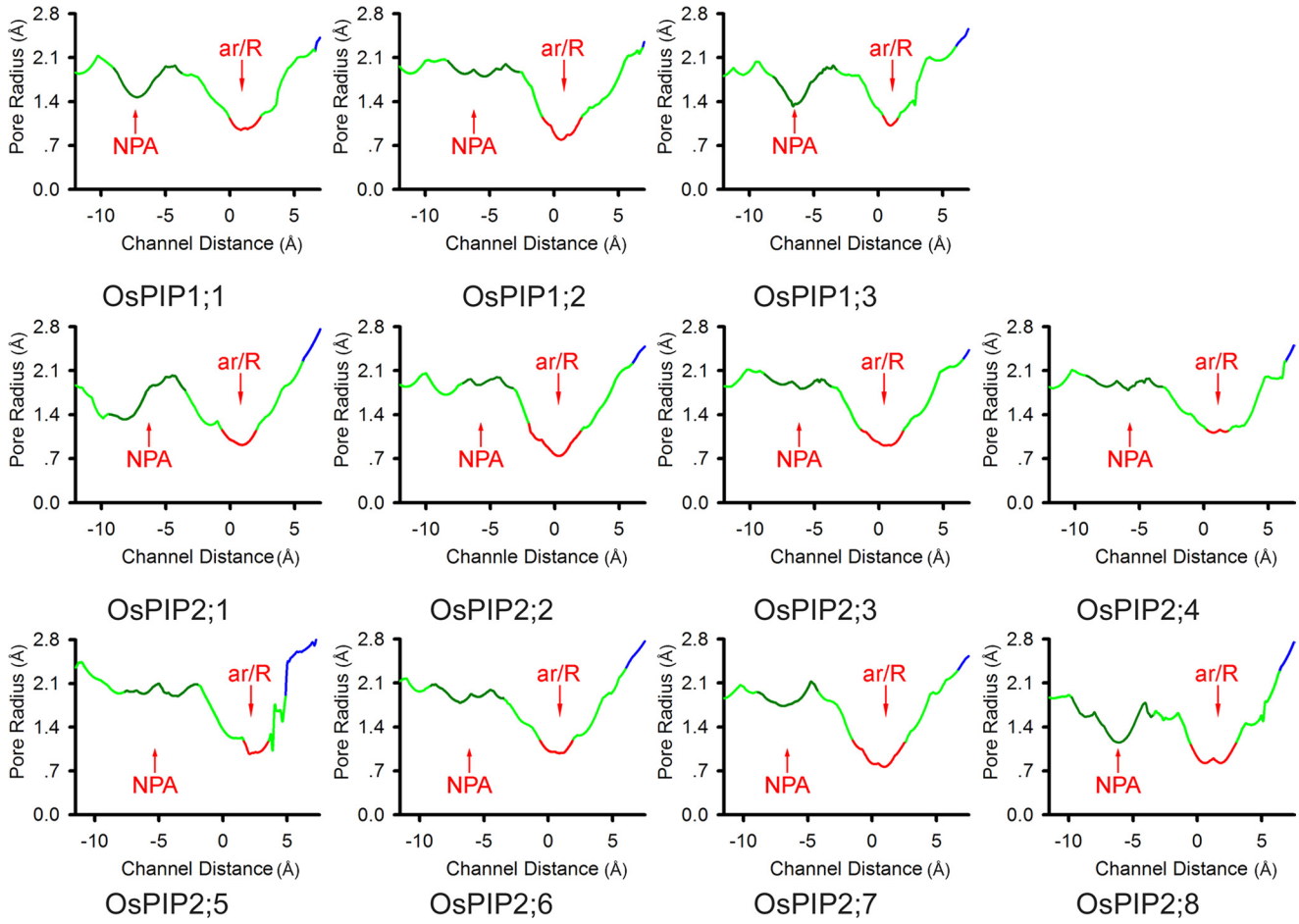

FIGURE 1. **Structure and pore radius of all OsPIP proteins.** The structure of each OsPIP was generated by GeneAtlas, and channel radius was calculated by HOLE. The pore radius was plotted in *blue* when the radius was >2.3 Å, in *red* when it was <1.15 Å, and in *green* when between 1.15 and 2.3 Å. The position of the NPA (*dark green*) and ar/R (*red*) regions is indicated.

side chain of the Phe[102] residue was also found in OsPIP1;1 A103V (Figs. 2*A* and 3*B*, *blue licorice*).

Functional Confirmation on Site-directed Mutagenesis—To test the functionality of the Ala/Ile(Val) site on P_f, two sets of measurements were performed in water transport activity and membrane localization using site-directed mutagenized OsPIPs.

Water Transport Activity—The above structural comparisons suggested that the water permeability that is supposedly higher in WT OsPIP2s than that in WT OsPIP1s could be reversed using Ala/Ile(Val) interchanged mutation. The P_f values of the AQPs were measured in *Xenopus* oocytes, using an osmotic permeation assay after intracellular injection of WT and mutated OsPIP1;1, OsPIP1;3, OsPIP2;3, and OsPIP2;7 cRNAs. The P_f was found to be higher in oocytes expressing WT OsPIP2s than in those expressing WT OsPIP1s (Fig. 4, *A–D*). It was also enhanced in both OsPIP1;1 and OsPIP1;3 mutants (Fig. 4, *A* and *B*) where the P_f value was 7.0-fold higher for OsPIP1;1 A103V than for OsPIP1;1 oocytes ($(1.61 \pm 0.54$ and $0.23 \pm 0.12) \times 10^{-2}$ cm/s, respectively, $p < 0.05$) or 2.2-fold higher for OsPIP1;3 A102V than for OsPIP1;3 oocytes ($(0.62 \pm 0.28$ and $0.28 \pm 0.16) \times 10^{-2}$ cm/s, respectively, $p < 0.05$). In contrast, both OsPIP2;3 and OsPIP2;7 mutants exhibited a reduced P_f as compared with their respective WTs (Fig. 4, *C* and *D*) with the P_f value of ($(1.12 \pm 0.34$ and $4.12 \pm 1.03) \times 10^{-2}$ cm/s, respectively) for OsPIP2;3 I98A and OsPIP2;3 (73% reduction; $p < 0.05$) or ($(2.55 \pm 1.15$ and $5.36 \pm 1.71) \times 10^{-2}$ cm/s, respectively) for OsPIP2;7 V95A and OsPIP2;7 (52% reduction, $p < 0.05$). These results indicated that the Ala/Ile(Val) site in OsPIPs dramatically affected the water transport activity.

Membrane Localization—To further test if the site-directed mutation affected the membrane localization of OsPIP proteins, GFP was fused at the C-terminal end of WT OsPIP1;1, OsPIP1;3, OsPIP2;3, and OsPIP2;7 and of their corresponding mutants, respectively. The expression and localization of the proteins in *Xenopus* oocytes membrane were visualized using laser confocal microscopy (Fig. 4*E*). AQP2 was used as a marker protein to show the membrane localization (Fig. 4*F*). The fluorescence intensity was measured, and Student's *t* test analysis showed that no significant difference in fluorescence intensity was found between WTs and mutated OsPIPs with one exception for OsPIP1;3A/V that yielded 50% lower intensity than that of OsPIP1;3 (Fig. 4*G*), indicating that the membrane localization of OsPIPs was not altered by site-directed mutagenesis and that the membrane targeting efficiency was declined in OsPIP1;3A/V. Even with relatively low membrane

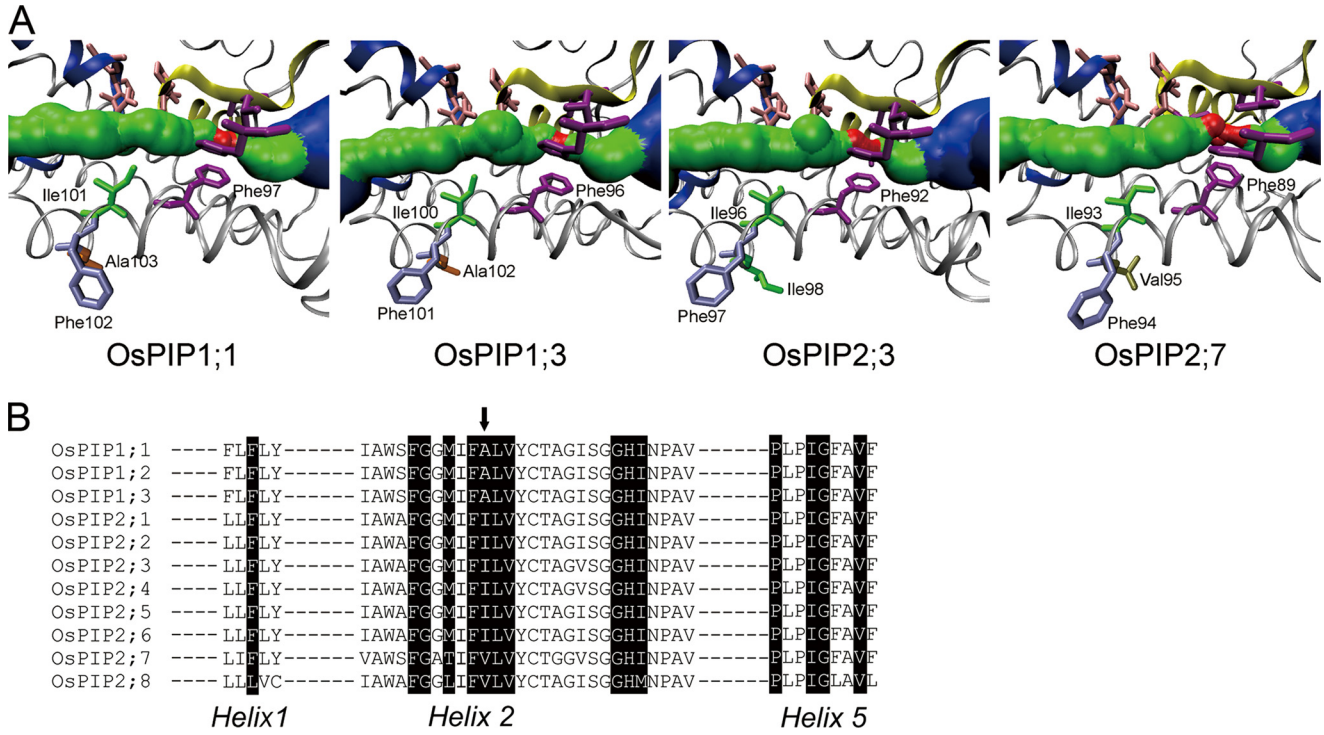

FIGURE 2. **Structure difference between OsPIP1s and OsPIP2s.** *A,* structures of OsPIP1;1, OsPIP1;3, OsPIP2;3, and OsPIP2;7.The helixes are shown as ribbons in *silver*, and loops B and E are illustrated as ribbons in *blue* and *yellow*, respectively. Two NPA motifs in loops B and E are presented as licorice in *pink*. Amino acids that constituted the ar/R region are shown as licorice in *purple*. The Ile residue at the NPA region is illustrated as licorice in *green*. Other residues on helix 2 discussed in the text are also indicated. *B,* part of sequence alignment of all OsPIPs. *Black boxes* showed the residues within 6 Å of Ile. The *arrow* indicated the conserved Ala/Ile(Val) site focused on in this study.

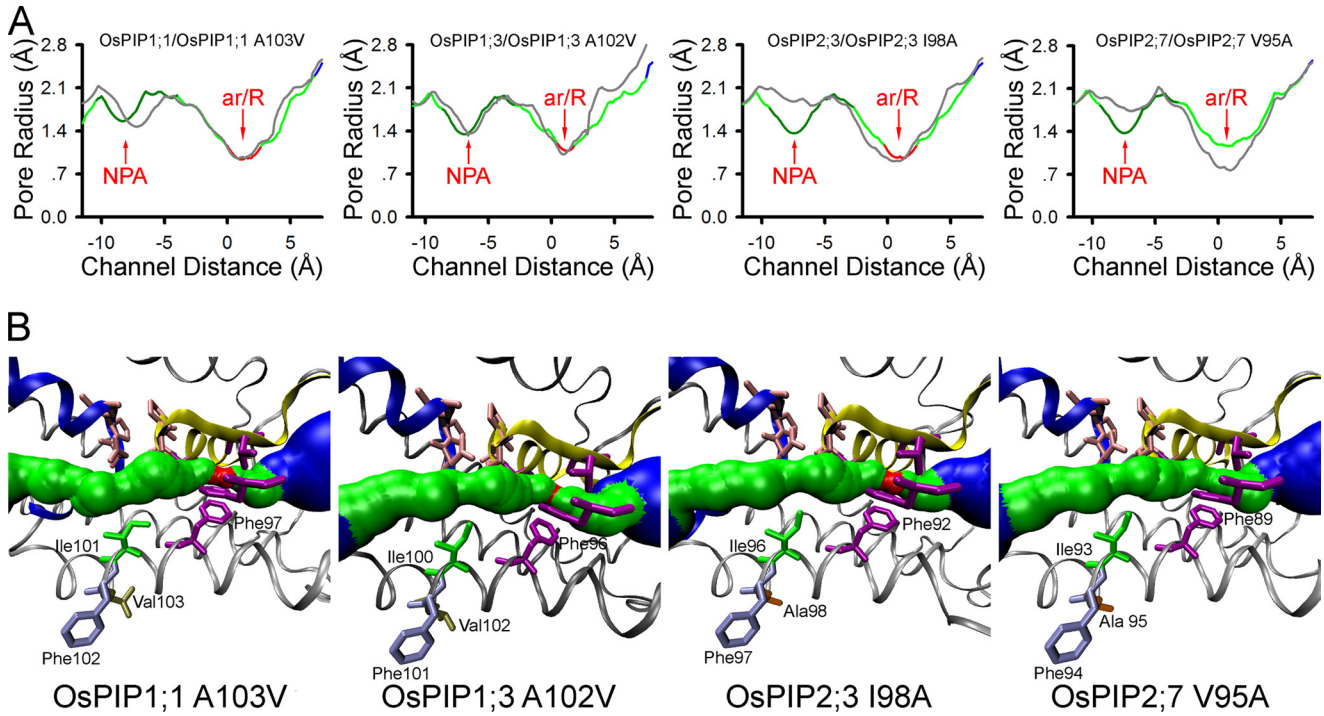

FIGURE 3. **Structure and pore radius of WT and mutated OsPIP proteins.** *A,* pore radii of four OsPIPs and their corresponding mutants are illustrated in *gray* and *colored lines*, respectively. *Dark green line* presents the difference in NPA region between WT and corresponding mutant OsPIPs. *B,* structures of OsPIP1;1 A103V, OsPIP1;3 A102V, OsPIP2;3 I98A, and OsPIP2;7 V95A. The orientation of Ile side chain induced the channel radius variation in OsPIP mutants. All the elements are shown in same color as in Figs. 1 and 2.

expression, high permeability was also found for OsPIP17; 3A/V. These results further supported the hypothesis that the Ala/Ile(Val) difference between the four WT OsPIPs and their respective mutants OsPIPs, rather than interfering with membrane localization, induced a real change in intrinsic water transport activity.

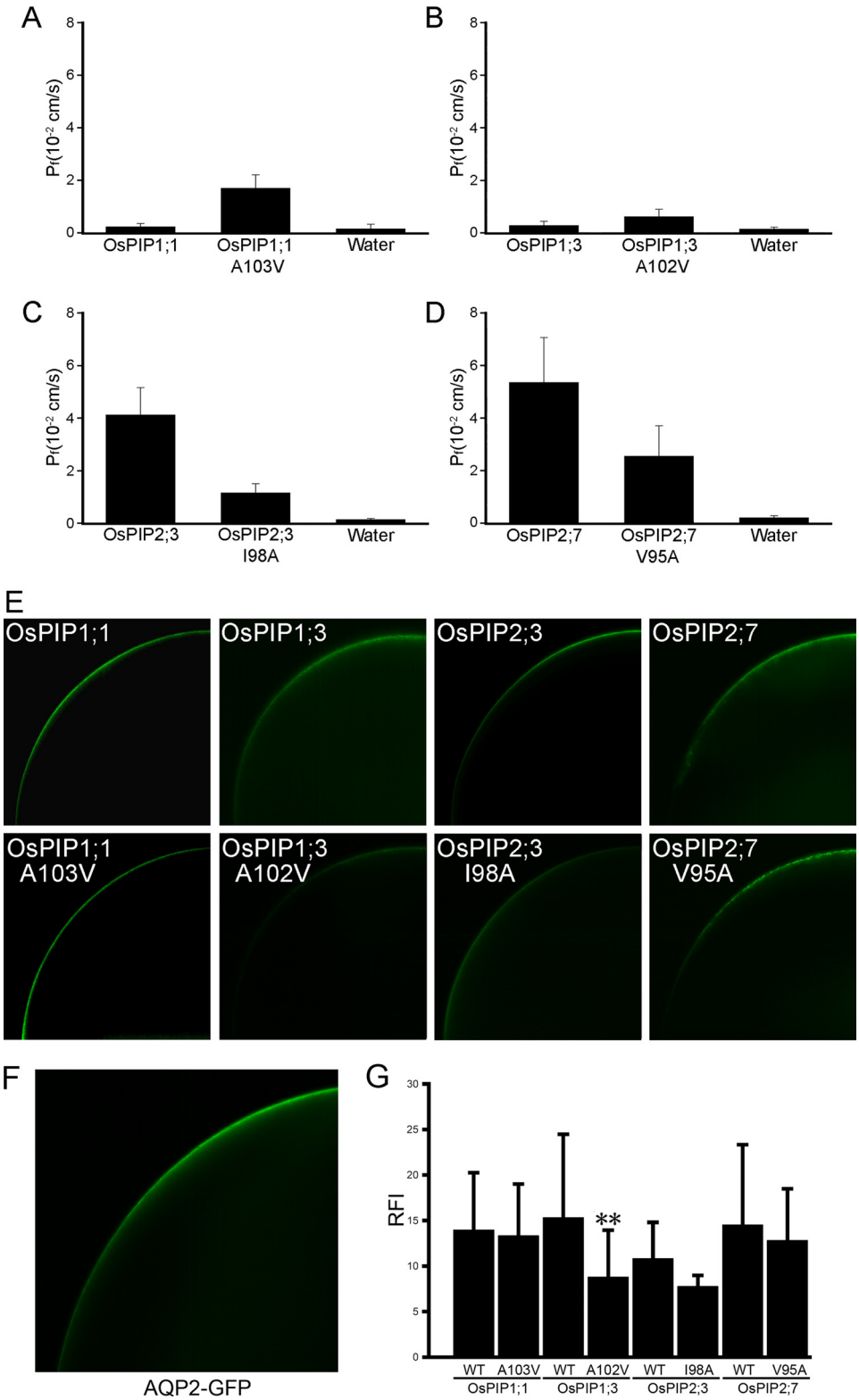

FIGURE 4. **Osmotic water permeability and protein location of WT and mutated OsPIPs.** *A–D, Xenopus* oocytes were injected with 23.5 nl of cRNA of WT or mutated OsPIPs or water (as control) and cultured for 48 h in ND96 solution. The P_f was plotted for OsPIP1;1 and OsPIP1;1 A103V (*A*), OsPIP1;3 and OsPIP1;3 A102V (*B*), OsPIP2;3 and OsPIP2;3 I98A (*C*), and OsPIP2;7 and OsPIP2;7 V95A (*D*). *E* and *F,* confocal microscope images were presented for oocytes injected with cRNA of the four OsPIPs and their mutants fused with GFP at the C terminus (*E*) together with the oocyte injected with cRNA of AQP2-GFP, showing the localization of AQP2 on the plasma membrane (*F*). *G,* estimation of expression levels of OsPIP constructs in injected oocytes. One-quarter of an oocyte was imaged by laser confocal microscopy and digitized using ImageJ software. Eight transmembrane boxes in a size of 100 × 1 pixels were selected along the membrane, and the *gray* values inside the box were measured and averaged to be the relative fluorescence intensity (*RFI*) of protein expression for that cell. The relative fluorescence intensity of the each WT and correspondent mutant PIP was statistically analyzed by Student's *t* test. Significant value relative to the WT is indicated: **, $p < 0.01$.

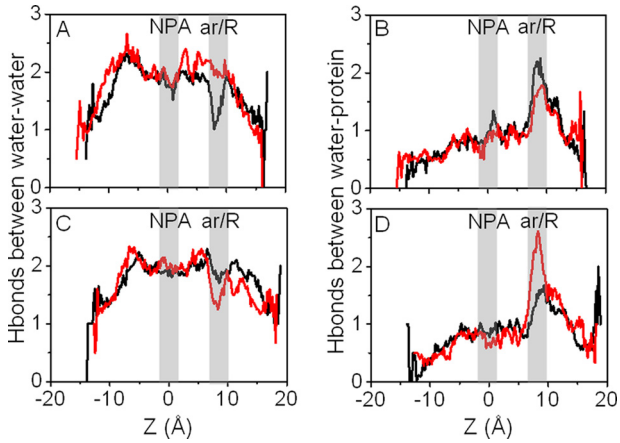

FIGURE 5. **Differences in channel water-water and water-protein interactions.** Channel water-water and water-protein interactions between WT (*black*) and mutant (*red*) OsPIPs are compared. Average number of H-bonds between a water molecule with its oxygen atom located along the *z* axis and its adjacent water molecules (*A* and *C*) and between the molecule and channel protein (*B* and *D*) are illustrated for OsPIP1;1 (*A* and *B*) and OsPIP2;7 (*C* and *D*). A hydrogen bond was defined as having donor-acceptor distance of <3.5 Å and a donor-hydrogen-acceptor angle of <45°. Data were collected from all channel water molecules during the entire equilibration process for every monomer and presented as group average with a bin size of 0.2 Å. The reference origin was denoted as the *Z* coordinate of the Ile^{101}-CD atom of OsPIP1;1 or Ile^{93}-CD atom of OsPIP2;7. The NPA motif and ar/R region are highlighted in *semitransparent gray stripes*.

Dynamic Structural Bases for Ala/Ile(Val) Site-related Functionality—MD simulations were performed to understand the dynamic structural bases of Ala/Ile(Val) functionality using WT and mutated OsPIP1;1 and OsPIP2;7.

Correlation of Water Permeability with Water-Water and Water-Protein Interactions—Monomeric P_f for WT OsPIPs and their mutants was estimated using the collective diffusion model described previously (38), where the diffusion coefficient of channel water was calculated in a time interval of 200 ps for the channel region of $-6 \leq Z \leq 12$ Å with $Z = 0$ at Ile^{101}-CD atom (the fourth carbon atom of Ile residue that is consistently named with CHARMM force field, similar tokens were used in the following) for OsPIP1;1 or of $-6 \leq Z \leq 15$ Å with $Z = 0$ at Ile^{93}-CD atom for OsPIP2;7. These analyses yielded P_f values (in 10^{-14} cm^3/s) of 2.18 ± 0.41 and 2.72 ± 0.52 for OsPIP1;1 and OsPIP1;1 A103V, respectively, and of 3.53 ± 0.58 and 2.91 ± 1.02 for OsPIP2;7 and OsPIP2;7 V95A, respectively. These results were in agreement with the above functional measurements that OsPIP1;1 A103V enhanced but OsPIP2;7 V95A reduced the P_f as compared with their respective WTs.

Water-water interactions promote water permeation, whereas water-protein interactions have the opposite effect. As exemplified in Fig. 5, *A* and *B*, stronger hydrogen bonding (H-bonding) in water-water interactions and weaker H-bonding in water-protein interactions were exhibited by OsPIP1;1 A103V (*red lines*), as compared with its WT (*black lines*). This further supported the observation that, as compared with OsPIP1;1, P_f was enhanced in OsPIP1;1 A103V. By contrast, OsPIP2;7 V95A exhibited, by comparison with WT OsPIP2;7, reduced water-water interactions and fostered water-protein interactions, in agreement with the reduction in P_f induced by the point mutation (Fig. 5, *C* and *D*, *red lines*). These results provided a global interpretation of structural bases for mutagenesis-induced changes in P_f.

Orientation and Stability of Side Chain of Key Residues—Differences in H-bond interactions appeared to localize at a narrow region between the 0 to +10 Å coordinates (Fig. 5), especially at two positions corresponding to the NPA (around ~0 Å) and ar/R regions (around ~10 Å) (Fig. 5, *gray stripes*). Residue orientation analyses for the two regions indicated that two key residues contributed to the differences. One was $Ile^{101/93}$ in OsPIP1;1/2;7 that pointed to the channel pore at the NPA region (Fig. 2*A*, *green licorice*) and the other was $Phe^{97/89}$ in OsPIP1;1/2;7 that constituted the ar/R region (Fig. 2*A*, *purple licorice*). The angle between $Ile^{101/93}$ vector (from atom $Ile^{101/93}$-CD to atom $Ile^{101/93}$-CG2 *or* CD → CG2 in short) or $Phe^{97/89}$ vector (from $Phe^{97/89}$-CD2 to $Phe^{97/89}$-CD1 *or* CD2 → CD1 in short) and the *z*-axis vector (parallel to water channel and pointing from the cytoplasmic to extracellular domain) was calculated to evaluate the orientation of side chain of the two key residues. It was found that Ile^{101} orientation was stable at ~127° for OsPIP1;1 A103V in three monomers (supplemental Fig. S2*B*) as compared with its unstable orientation for OsPIP1;1 with varied angles (supplemental Fig. S2*A*). In contrast Ile^{93} orientation in OsPIP2;7 fluctuated up to ~68° (supplemental Fig. S2*C*) as compared with its stable orientation at ~127° for OsPIP2;7 V95A (supplemental Fig. S2*D*). Such orientation fluctuation affected P_f because both Ile^{101} and Ile^{93} are pore-forming residues. A typical evolution analysis (Fig. 6*A*) indicated that the side chain of Ile^{101} residue in OsPIP1;1 pointed to the channel pore at 1.8 ns (~68°) to interrupt the continuity of the water molecule file, moved away at 3.0 ns (~127°) to favor water file formation, and confined its orientation at 4.2 ns (~150°) to induce an intermediate opening (Fig. 6*A*, *insets*). This was in agreement with different orientations of Ile side chain at different pore radii found in homology modeling (Fig. 2). This orientation instability hindered water molecule movements in the vicinity of Ile^{101} residue and resulted in weaker water-water and stronger water-protein interactions.

Another region presenting different H-bond interactions around ~10 Å corresponded to the ar/R region (Fig. 5, *gray stripes*). The side chain of $Phe^{97/89}$ residue in OsPIP1;1/2;7, one of the four residues constituting the ar/R region, oriented more stably at ~38° for OsPIP1;1 or at ~46–88° for OsPIP2;7 than that at ~38–120° for OsPIP1;1 A103V or at ~7–141° for OsPIP2;7 V95A (supplemental Fig. S3). The distinct nature of orientation and stability between the two OsPIPs affected the conformation of the ar/R region and resulted in a P_f difference. Typically, the Phe^{97} side chain in OsPIP1;1 A103V pointed to the channel pore (~38°) followed by an open orientation (~62° and even ~80°), and finally moved away from the ar/R region (*insets*) (Fig. 6*B* and supplemental Fig. S3, *A* and *B*). This reorientation of hydrophobic Phe^{97} residue favored the passage of water molecules and resulted in stronger water-water and weaker water-protein interactions, as compared with those in OsPIP1;1. High orientation fluctuation of Phe^{89} side chain in OsPIP2;7 V95A indicated that the instability interrupted the continuity of the water file and resulted in weaker water-water and stronger water-protein interactions,

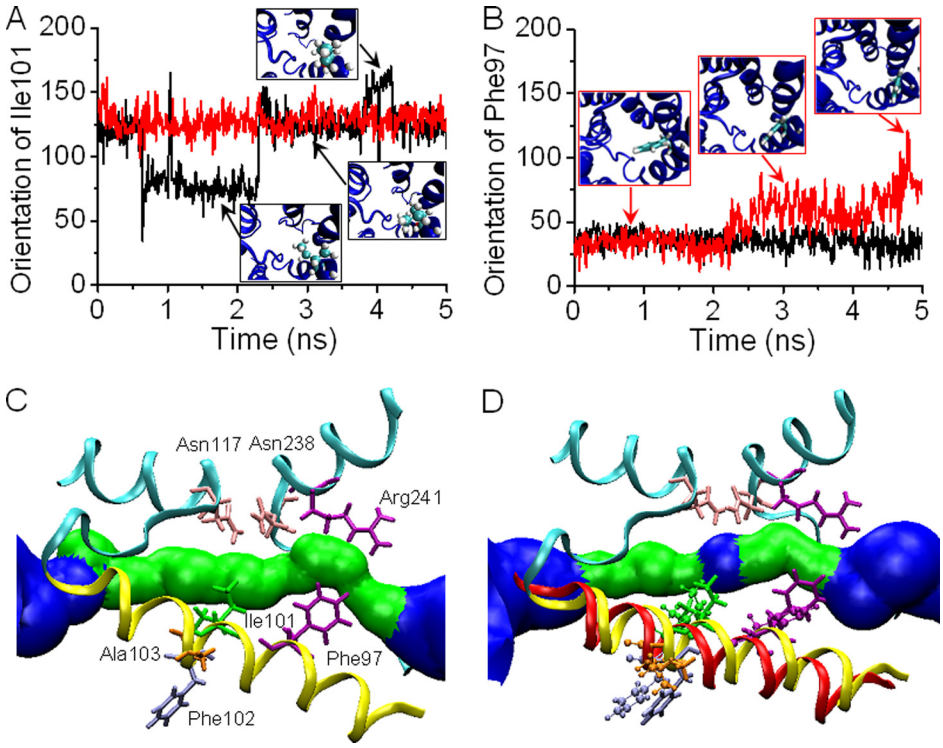

FIGURE 6. **Orientation of the key residues and helix 2 in OsPIP1;1.** *A* and *B*, orientation evolution of the Ile^{101} (*A*) or Phe^{97} (*B*) side chain for a typical monomer are presented as the time course of the angle between the Ile^{101} (CD → CG2) or Phe^{97} (CD2 → CD1) vector and the *z*-axis vector in OsPIP1;1 (*black*) and OsPIP1;1 A103V (*red*). Also plotted are typical snapshots at specific moments (*insets* in *cyan CPK* or *sticks*). Background channels are presented in *blue* as control. *C* and *D*, typical monomer snapshot was illustrated for OsPIP1;1 alone (*C*) and for both OsPIP1;1 and OsPIP1;1 A103V at 4.86 ns (*D*). Channel structure was partially represented as a *ribbon* with the helix 2 (*yellow*), two NPA motifs with the corresponding half-helices, and loops (*cyan*), and channel radius profile. Two Asn from the NPA motif, an Arg from the ar/R region, and the residues (Ala^{103}, Phe^{102}, Ile^{101}, and Phe^{97}) pertinent to the proposed model are illustrated as licorice in the same color as in Figs. 2*A* and 3*B*. Also plotted in *D* are the orientation changes in helix 2 (*red ribbon*) and the corresponding residues (*CPK* presentation) with the channel radius profile for OsPIP1;1 A103V.

although no significant difference in orientation angles was found (supplemental Fig. S3, *C* and *D*). It was also observed that the Ile^{93} orientation in OsPIP2;7 (supplemental Fig. S2*A*) as compared with that in OsPIP2;7 V95A (supplemental Fig. S2*B*) seemed not to be favorable for water permeation. In particular, slightly weaker water-water and stronger water-protein interactions were found around in the NPA region in OsPIP2;7 as compared with OsPIP2;7 V95A (Fig. 5, *C* and *D*). In fact, orientation stability of another residue (Phe^{89}) was involved, and in combination with Ile^{93} orientation, it could account for the fact that the P_f was reduced in OsPIP2;7 V95A. Taken together, the analyses of side chain orientation and stability confirmed the above observations that P_f was enhanced for OsPIP1;1 A103V but reduced for OsPIP2;7 V95A.

Orientation of Helix 2—The two key residues discussed above, Ile^{101} and Phe^{97} of OsPIP1;1 and Ile^{93} and Phe^{89} of OsPIP2;7, are both located in the same helix 2 (Gly^{92}–Ile^{111} for OsPIP1;1 or Gly^{84}–Val^{103} for OsPIP2;7). They are, however, separated by several residues from the mutated site (Ala^{103} in OsPIP1;1 and Val^{95} in OsPIP2;7) (Figs. 2*A* and 3*B*). One possible mechanism for orientation changes induced by punctual mutations at a distant site is that the two mutations (A103V or V95A) triggered a re-orientation of helix 2 thereby driving a distant reorientation of Ile$^{101/93}$ and Phe$^{97/89}$ side chains. To test this, the angle between helix 2 vector (Leu^{104}-CA → Ala^{94}-CA for OsPIP1;1 or Leu^{96}-CA → Ala^{86}-CA for OsPIP2;7) and the *Z*-axis vector was calculated. The mean angle was enhanced for OsPIP1;1 A103V (36.8 ± 0.8°, *red line*) as compared with that for OsPIP1;1 (34.8 ± 0.8°, *black line*) (Fig. 7*A*) but reduced for OsPIP2;7 V95A (37.7 ± 1.0°, *red line*) when compared with that of OsPIP2;7 (39.9 ± 0.8°, *black line*) (Fig. 7*B*). This indicated that the orientation change of helix 2 (Fig. 7, *C* and *D*) was positively correlated with those of Ile$^{101/93}$ and Phe$^{97/89}$ residues for both WT and mutated OsPIPs (supplemental Figs. S2 and S3). Specifically, the enhancement or reduction of the angle was induced by reducing the motion freedom of the Phe^{102} residue in OsPIP1;1 A103V or increasing the freedom of Phe^{94} in OsPIP2;7 V95A (supplemental Fig. S4). Thus, the analysis confirmed the prediction that the orientation of helix 2 played a role to transfer the conformational change from the mutated site to the constraint regions.

In summary, we proposed a model to interpret how site-directed Ala-Val mutation regulated the P_f of OsPIPs. Typically, OsPIP1;1 A103V mutation drove a helix 2 orientation change (Fig. 6*D*, *yellow* for WT and *red* for A103V), which induced stable and favorable orientations of Ile^{101} residue at the NPA region and of Phe^{97} residue at the ar/R region (Fig. 6, *C* and *D*). Such orientation change opened the channel pore, widened the radius profile, and combined with a well formed water molecule file, enhanced the P_f. By contrast, the converse effect for OsPIP2;7 V95A mutation was demonstrated by opposite pathways (supplemental Fig. S5).

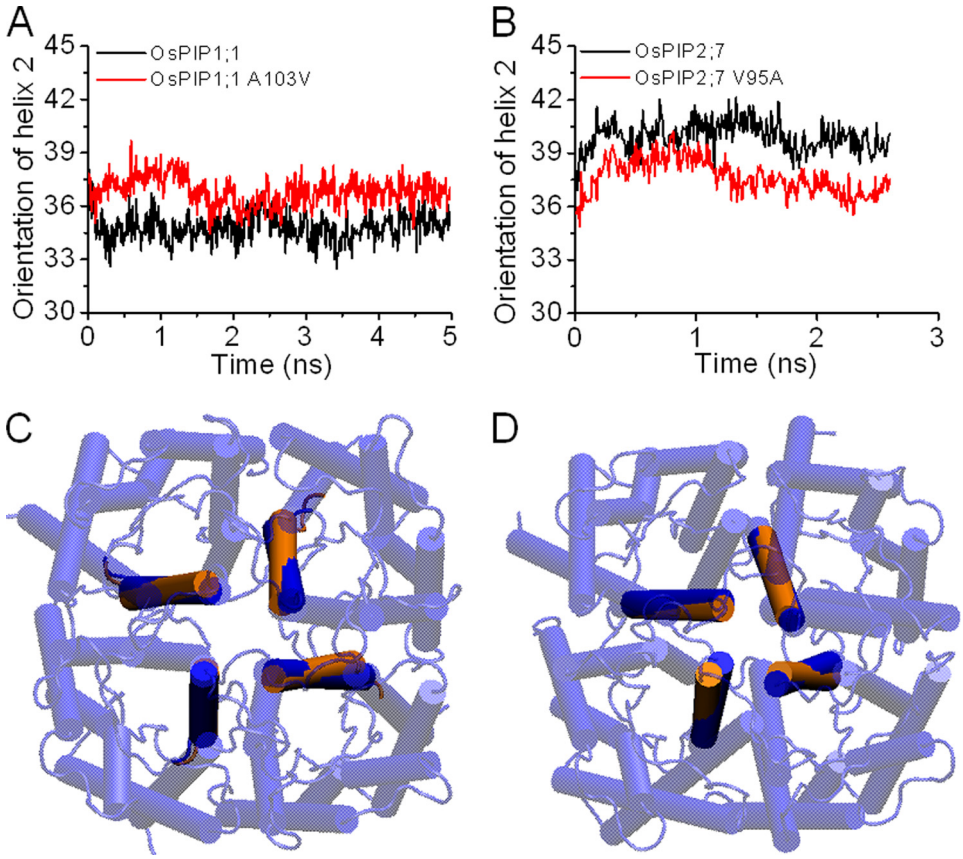

FIGURE 7. **Helix 2 orientation difference between WT and mutant.** *A* and *B,* tetramer average of helix 2 orientation evolved during the equilibration process of OsPIP1;1 (*A*) and OsPIP2;7 (*B*). The helix 2 orientation was denoted by the angle between helix 2 vector (Leu^{104}-CA → Ala^{94}-CA for OsPIP1;1 or Leu^{96}-CA → Ala^{86}-CA for OsPIP2;7) and *z*-axis vector. *C* and *D,* referred visualization of conformational comparison of helix 2 was illustrated by structurally superimposing of the wild type (*blue*) and mutant (*orange*) for OsPIP1;1 (*C*) and OsPIP2;7 (*D*). Full channel structure was shown with *blue* transparent presentation for demonstrating channel pores.

DISCUSSION

AQPs are crucial for the transport of water and/or other small solutes across cell membranes, and their functionality is defined by specific gating, selectivity, and permeability properties. Several mechanisms have been proposed to determine the activity of AQPs in plant cells via co- and post-translational modification, gating, trafficking, as well as the combinatorial regulations (within two different types of AQPs) (1). Plant AQPs can be gated by protons, divalent cations, and phosphorylation, and several recent studies have provided novel insights into the molecular mechanisms involved. Structure-function analyses in plant and animal AQPs have also shown that their distinct molecular selectivity and ion exclusion are determined in large part by the ar/R and NPA constrictions. For rat AQP1, replacement of the ar/R components Phe^{56} and His^{180} together may enlarge the maximal diameter of the ar/R constriction by 3-fold and enable glycerol and urea to pass (23). The goal of this study was to identify the key residue(s) for the P_f difference between OsPIP1s and OsPIP2s and to understand their corresponding structural bases at a single amino acid level.

In this study, selection of candidate residue(s) was achieved by identifying the conserved residue(s) from three-dimensional structural comparison between OsPIP1s and OsPIP2s (Fig. 2). The impact of the selected Ala/Ile(Val) residue on P_f of OsPIPs was then tested by structural differences and distinct pore radii using the reconstructed three-dimensional structure via virtual homology modeling, which was further validated by interchanging the residue between OsPIP1s and OsPIP2s (Fig. 3). PIP channel analysis allowed identification of structure difference for PIP1s and PIP2s, *i.e.* the extra constriction at the NPA region of PIP1s. Exceptions were found for OsPIP1;2, which exhibits PIP2 pore feature, and OsPIP2;1, OsPIP2;8 showed PIP1 pore feature (Fig. 1). Because the P_f of the OsPIP1;2 and OsPIP2;1 was consistent with their own subgroup (9), the Ala/Ile(Val) residue might be one of the important residues that influence the pore structure of the PIPs and hence the water permeation. We cannot rule out that other structure characters influence water permeation besides the major constriction at the NPA and ar/R regions, which was consistent with the result that OsPIP2;3 I98A and OsPIP2;7 V95A mutant proteins were not impermeable to water as OsPIP1s (Fig. 4, *C* and *D*). Specific pore feature, *e.g.* the cytoplasmic constriction in AQP0 (24, 25), and the key residues, *e.g.* the Ile or Val in RsPIPs located on loop E close to the extracellular space, may influence the water permeation through AQPs (12). On the other hand, homology modeling of the specific proteins need to be refined manually to fit the biological character. In addition, Ala/Ile(Val) site difference showed extensive conservation not only in rice PIPs but also

in PIPs from other plant species (supplemental Fig. S1*B*), suggesting that it is physiologically important for the large numbered, diverse AQP family in plants.

The existence of a large number and divergent AQPs in plant genomes might be a result of adaptation to the different water and ionic environments from the sea during the landing process in plant evolution. The Ala/Ile(Val) residue difference was found to be conservative in all higher plant PIPs (supplemental Fig. S1*B*) as well as in PIPs from *Physcomitrella patens* (supplemental Fig. S1*C*), which is Ala in PpPIP1s and Val in PpPIP2s with one exception of Thr in PpPIP1;3. *P. patens* was diverged from the lineage leading to higher plants ~443–490 million years ago just before the evolution of vascular plants (10, 39). It can be imagined that the development of a subgroup of PIPs with low water permeability (*i.e.* PIP1s) might be responsible for fine-tuning the cellular water transport and protecting the terrestrial plants from water loss. The functionality of Ala/Ile(Val) residue in regulating P_f was then confirmed using an osmotic permeation assay, and it was concluded that the interchanging of Ala/Ile(Val) residue between OsPIP1 and OsPIP2 reversed the P_f (Fig. 4, *A–D*). An alternative possibility, however, was that the various AQPs under investigation differed in their ability to traffic to the oocyte plasma membrane. Such a mechanism was determined to explain the apparent lack of activity of maize PIP1 isoforms after expression in *Xenopus* oocytes (40). Here, our results excluded the possibility by indicating that the OsPIP molecules were functionally located on the cell membrane for both WT and mutated OsPIPs and that the membrane localization of the protein was not significantly altered by site-directed mutagenesis (Fig. 4, *E–G*). In agreement with the previous report, OsPIP1;2 was found to be expressed and trafficked to the yeast membrane with similar efficiency as OsPIP2s, but the water transport activity of OsPIP1;2 was smaller than OsPIP2s (9). Our data further affirmed that OsPIP1s are less permeable to water than OsPIP2s partly due to the Ala/Ile(Val) difference.

MD simulations are advantageous in elucidating the dynamics of AQP activities in an accessible time scale of water transport across the channel (~1 ns) and in unraveling the evolution of conformational stability and the water-water and water-protein interactions. In this study, a model was proposed from MD simulations that the Ala/Ile(Val) mutation induced the orientation change of helix 2 followed by conformational change of $Ile^{101/93}$ residue at the NPA region and of $Phe^{97/89}$ residue at the ar/R region. This, in turn, enhanced water-water interactions and reduced water-protein interactions in OsPIP1;1 A103V or vice versa in OsPIP2;7 V95A (Figs. 5–7 and supplemental Figs. S2–S4). Our simulations correlated P_f value with water-water and water-protein interactions on the viewpoint of conformational diversity and stability of key residues, which bridged the structural changes and functional measurements (27, 28). This is because the orientation determines the energy barrier, and the instability interrupts the constancy of water motion, thereby affecting the dynamic process of water transport and the statistics of water-water and water-protein interactions. Overall, our analyses provided structural bases for understanding the role of Ala/Ile(Val) site in P_f.

It has been known that ar/R region determines the selectivity of AQP, and the mutation of its residue modified the channel property (18). In this study, the Ala/Ile(Val) mutation induced the orientation change of $Phe^{97/89}$ residue in the ar/R region and, in turn, enhanced or reduced P_f in OsPIP1s or OsPIP2s. It still remains unknown whether the mutation affects the selectivity of OsPIP1s and/or OsPIP2s or whether there is a synergetic or competing mechanism between the selectivity and the permeability. It is possible that PIP1s are less permeable to water because they can transport other molecules, *e.g.* CO_2 (41). It should also be pointed out that there are several other amino acids that are conserved within PIP1 and PIP2 groups but not between the isoforms belonging to the two different subgroups. The mutations in any of these amino acids might also influence the function of the isoforms within these groups. Further investigations are still required to address these issues, which are beyond of the scope of this study.

Acknowledgments—We thank Dr. C. Maurel and Prof. Y. Kitagawa for providing the AQP1 and AQP2 cDNAs. We thank Dr. C. Maurel, Prof. D. Lane, and Prof. W. H. Jiang for critical reading of the manuscript. We thank Prof. L. Li and co-workers and X. Wang for help in analysis of the PIPs-GFP expression in oocytes. MD simulations were performed at the Supercomputing Center of the Chinese Academy of Sciences.

REFERENCES

1. Maurel, C., Verdoucq, L., Luu, D. T., and Santoni, V. (2008) *Annu. Rev. Plant Biol.* **59,** 595–624
2. Kjellbom, P., Larsson, C., Johansson, I. I., Karlsson, M., and Johanson, U. (1999) *Trends Plant Sci.* **4,** 308–314
3. Fujiyoshi, Y., Mitsuoka, K., de Groot, B. L., Philippsen, A., Grubmüller, H., Agre, P., and Engel, A. (2002) *Curr. Opin. Struct. Biol.* **12,** 509–515
4. Tajkhorshid, E., Nollert, P., Jensen, M. Ø., Miercke, L. J., O'Connell, J., Stroud, R. M., and Schulten, K. (2002) *Science* **296,** 525–530
5. Biela, A., Grote, K., Otto, B., Hoth, S., Hedrich, R., and Kaldenhoff, R. (1999) *Plant J.* **18,** 565–570
6. Chaumont, F., Barrieu, F., Jung, R., and Chrispeels, M. J. (2000) *Plant Physiol.* **122,** 1025–1034
7. Chaumont, F., Barrieu, F., Wojcik, E., Chrispeels, M. J., and Jung, R. (2001) *Plant Physiol.* **125,** 1206–1215
8. Dixit, R., Rizzo, C., Nasrallah, M., and Nasrallah, J. (2001) *Plant Mol. Biol.* **45,** 51–62
9. Sakurai, J., Ahamed, A., Murai, M., Maeshima, M., and Uemura, M. (2008) *Plant Cell. Physiol.* **49,** 30–39
10. Danielson, J. A., and Johanson, U. (2008) *BMC Plant Biol.* **8,** 45
11. Wallace, I. S., and Roberts, D. M. (2004) *Plant Physiol.* **135,** 1059–1068
12. Suga, S., and Maeshima, M. (2004) *Plant Cell. Physiol.* **45,** 823–830
13. Sui, H., Han, B. G., Lee, J. K., Walian, P., and Jap, B. K. (2001) *Nature* **414,** 872–878
14. Murata, K., Mitsuoka, K., Hirai, T., Walz, T., Agre, P., Heymann, J. B., Engel, A., and Fujiyoshi, Y. (2000) *Nature* **407,** 599–605
15. Gonen, T., Cheng, Y., Sliz, P., Hiroaki, Y., Fujiyoshi, Y., Harrison, S. C., and Walz, T. (2005) *Nature* **438,** 633–638
16. Gonen, T., Sliz, P., Kistler, J., Cheng, Y., and Walz, T. (2004) *Nature* **429,** 193–197
17. Nyirenda, T. E., Harries, A. D., Gausi, F. K., Ito, K., Kemp, J. R., Squire, B. S., Godfrey-Faussett, P., and Salaniponi, F. M. (2004) *Int. J. Tuberc. Lung Dis.* **8,** 1089–1094

18. Fu, D., Libson, A., Miercke, L. J., Weitzman, C., Nollert, P., Krucinski, J., and Stroud, R. M. (2000) *Science* **290,** 481–486
19. Savage, D. F., Egea, P. F., Robles-Colmenares, Y., O'Connell, J. D., 3rd, and Stroud, R. M. (2003) *PLoS Biol.* **1,** E72
20. Lee, J. K., Kozono, D., Remis, J., Kitagawa, Y., Agre, P., and Stroud, R. M. (2005) *Proc. Natl. Acad. Sci. U.S.A.* **102,** 18932–18937
21. Törnroth-Horsefield, S., Wang, Y., Hedfalk, K., Johanson, U., Karlsson, M., Tajkhorshid, E., Neutze, R., and Kjellbom, P. (2006) *Nature* **439,** 688–694
22. Kong, Y., and Ma, J. (2001) *Proc. Natl. Acad. Sci. U.S.A.* **98,** 14345–14349
23. Beitz, E., Wu, B., Holm, L. M., Schultz, J. E., and Zeuthen, T. (2006) *Proc. Natl. Acad. Sci. U.S.A.* **103,** 269–274
24. Jensen, M. Ø., Dror, R. O., Xu, H., Borhani, D. W., Arkin, I. T., Eastwood, M. P., and Shaw, D. E. (2008) *Proc. Natl. Acad. Sci. U.S.A.* **105,** 14430–14435
25. Han, B. G., Guliaev, A. B., Walian, P. J., and Jap, B. K. (2006) *J. Mol. Biol.* **360,** 285–296
26. Smolin, N., Li, B., Beck, D. A., and Daggett, V. (2008) *Biophys. J.* **95,** 1089–1098
27. Hashido, M., Ikeguchi, M., and Kidera, A. (2005) *FEBS Lett.* **579,** 5549–5552
28. Hashido, M., Kidera, A., and Ikeguchi, M. (2007) *Biophys. J.* **93,** 373–385
29. Kitson, D. H., Badretdinov, A., Zhu, Z. Y., Velikanov, M., Edwards, D. J., Olszewski, K., Szalma, S., and Yan, L. (2002) *Brief. Bioinform.* **3,** 32–44
30. Humphrey, W., Dalke, A., and Schulten, K. (1996) *J. Mol. Graph.* **14,** 27–38
31. Smart, O. S., Neduvelil, J. G., Wang, X., Wallace, B. A., and Sansom, M. S. (1996) *J. Mol. Graph.* **14,** 354–360, 376
32. Edgar, R. C. (2004) *Nucleic Acids Res.* **32,** 1792–1797
33. Daniels, M. J., Mirkov, T. E., and Chrispeels, M. J. (1994) *Plant Physiol.* **106,** 1325–1333
34. Weig, A., Deswarte, C., and Chrispeels, M. J. (1997) *Plant Physiol.* **114,** 1347–1357
35. Zhang, R. B., and Verkman, A. S. (1991) *Am. J. Physiol.* **260,** C26–C34
36. Phillips, J. C., Braun, R., Wang, W., Gumbart, J., Tajkhorshid, E., Villa, E., Chipot, C., Skeel, R. D., Kalé, L., and Schulten, K. (2005) *J. Comput. Chem.* **26,** 1781–1802
37. MacKerell, A. D., Bashford, D., Bellott, M., Dunbrack, R. L., Evanseck, J. D., Field, M. J., Fischer, S., Gao, J., Guo, H., Ha, S., Joseph-McCarthy, D., Kuchnir, L., Kuczera, K., Lau, F. T. K., Mattos, C., Michnick, S., Ngo, T., Nguyen, D. T., Prodhom, B., Reiher, W. E., Roux, B., Schlenkrich, M., Smith, J. C., Stote, R., Straub, J., Watanabe, M., Wiorkiewicz-Kuczera, J., Yin, D., and Karplus, M. (1998) *J. Phys. Chem. B* **102,** 3586–3616
38. Zhu, F., Tajkhorshid, E., and Schulten, K. (2004) *Phys. Rev. Lett.* **93,** 224501
39. Zardoya, R. (2005) *Biol. Cell.* **97,** 397–414
40. Fetter, K., Van Wilder, V., Moshelion, M., and Chaumont, F. (2004) *Plant Cell.* **16,** 215–228
41. Uehlein, N., Lovisolo, C., Siefritz, F., and Kaldenhoff, R. (2003) *Nature* **425,** 734–737

SUPPLEMENTARY INFORMATION

Accession Numbers

Sequence data for this article can be found in the GenBank data libraries under accession numbers: OsPIP1;1 (BAD27775), OsPIP1;2 (CAE01842), OsPIP1;3 (BAD22920), OsPIP2;1 (BAC15868), OsPIP2;2 (BAD23735), OsPIP2;3 (CAD41442), OsPIP2;4 (BAC16113), OsPIP2;5 (BAC16116), OsPIP2;6 (CAE05002), OsPIP2;7 (BAD46581) and OsPIP2;8 (AAP44741), BoPIP1b1 (AAG23179), BoPIP1b2 (AAG23180), HvPIP1;6 (CAA54233), MipA (AAB09747), MipB (AAA93521), MpPIP1;1 (BAD90696), NtAQP1 (CAA04750), NtPIP1;1 (AAL33585), LeAQP2 (AAF44085), OePIP1;1 (ABB13429), PoPIP1;1 (CAC85292), PsPIP1;1 (P25794), PvPIP1 (AAB72149), RsPIP1A (BAA32777), RsPIP1B (BAA92258), RsPIP1C (BAA92259), TgPIP1;1 (BAG68659), TgPIP1;2 (BAG68660), ZmPIP1;1 (Q41870), ZmPIP1;2 (Q9XF59), AtPIP2;3 (P30302), AtPIP2;7 (P93004), HvPIP2;1 (BAE02729), JcPIP2 (ABM54183), JrPIP2;1 (AAO39007), MpPIP2;1 (BAD90697) NtPIP2;1 (AAL33586) OePIP2;1 (ABB13430), PsPIP2;1 (CAB45651), PvPIP2;2 (ABU94630), PvPIP2;3 (ABU94631), RcPIP2;1 (CAE53883), RsPIP2A (BAA32778), RsPIP2B (BAA92260), RsPIP2C (BAA92261), SoPIP2;1 (AAA99274), TgPIP2;1 (BAG68661), TgPIP2;2 (BAG68662), ZmPIP2;1 (Q84RL7), ZmPIP2;4 (Q9ATM6), ZmPIP2;5 (Q9XF58) PpPIP1;1 (AAY83359), PpPIP1;2 (EDQ66794), PpPIP1;3 (EDQ53644), PpPIP2;1 (AAS72892), PpPIP2;2 (AAS72893), PpPIP2;3 (AAY83358) and PpPIP2;4 (XP001769800).

System build-up and equilibration in MD simulations

The channel monomer of each simulation system was based on their respective monomeric homology models. The channel tetramer was built by superposing the model structure of each monomer to the 1J4N template after sequence alignment, and tuning the water channel parallel to the *Z*-axis which points from the cytoplasmic to extracellular domain. Energy minimization and system heating were performed before the equilibration process. Here energy minimization was started with 10,000 steps of lipid bilayer optimization and an additional 10,000 steps to include more atoms of water and neutralized ions, followed by 30,000 steps with only the protein backbone fixed. The heating process from 0 to 300 *K* was performed through 30 *K* increment every 5 *ps*. After 500 *ps* protein backbone-constrained equilibration, free equilibrations for both OsPIP1;1 and OsPIP1;1 A103V (5 *ns*) and for OsPIP2;7 (2.6 *ns*) or OsPIP2;7 V95A (3.2 *ns*) were done under NPT ensemble conditions (300 *K* and 1 *atm*). The 300 *K* heat bath was controlled using a Langevin thermostat, and the 1 *atm* pressure was manipulated by the Nosé-Hoover Langevin piston method.

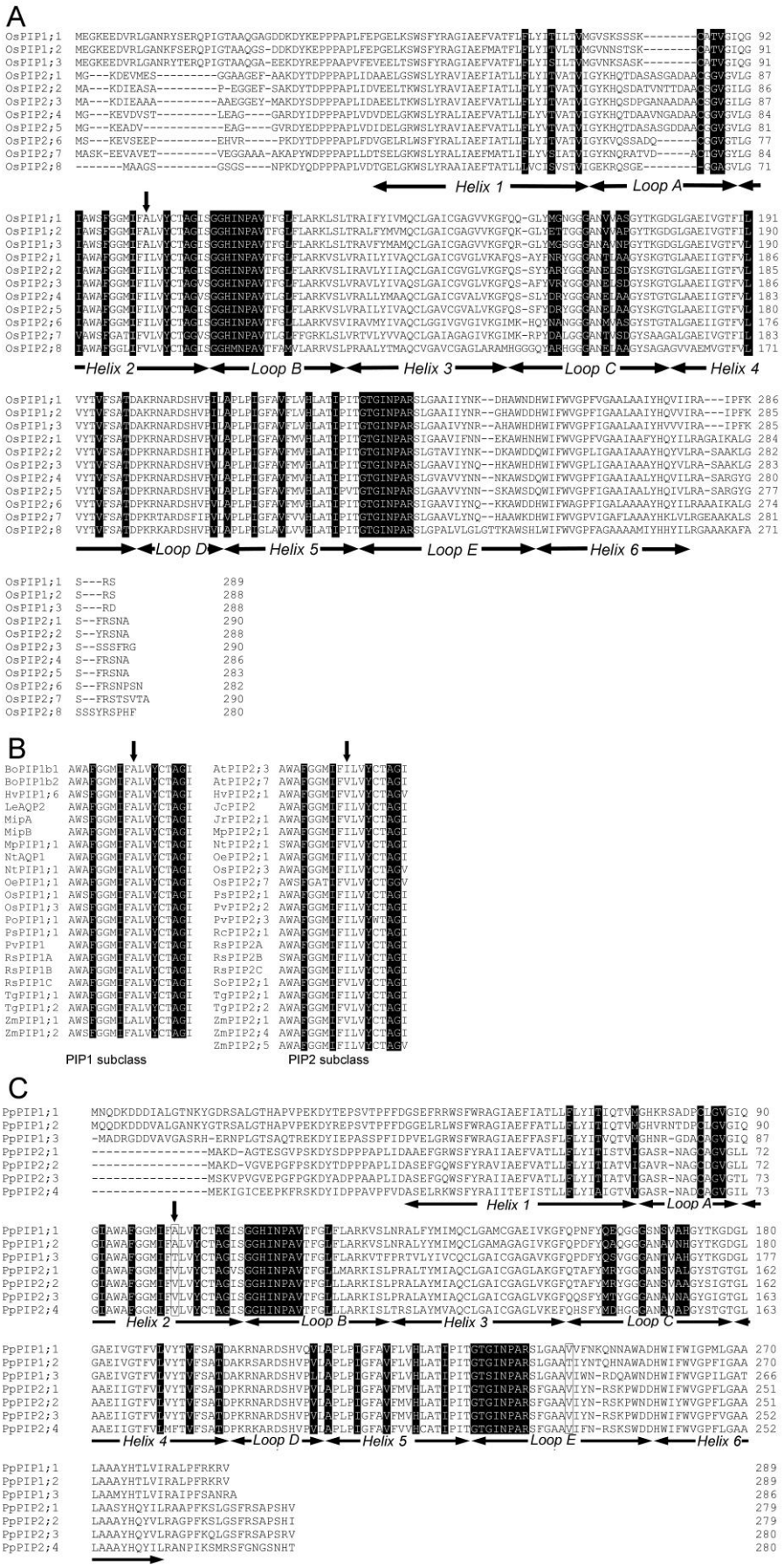
A
OsPIP1;1
OsPIP1;2
OsPIP1;3
OsPIP2;1
OsPIP2;2
OsPIP2;3
OsPIP2;4
OsPIP2;5
OsPIP2;6
OsPIP2;7
OsPIP2;8
Helix 1
Loop A
Helix 2
Loop B
Helix 3
Loop C
Helix 4
Loop D
Helix 5
Loop E
Helix 6
B
BoPIP1b1
BoPIP1b2
HvPIP1;6
LeAQP2
MipA
MipB
MpPIP1;1
NtAQP1
NtPIP1;1
OePIP1;1
OsPIP1;1
OsPIP1;3
PoPIP1;1
PsPIP1;1
PvPIP1
RsPIP1A
RsPIP1B
RsPIP1C
TgPIP1;1
TgPIP1;2
ZmPIP1;1
ZmPIP1;2
AtPIP2;3
AtPIP2;7
HvPIP2;1
JcPIP2
JrPIP2;1
MpPIP2;1
NtPIP2;1
OePIP2;1
OsPIP2;3
OsPIP2;7
PsPIP2;1
PvPIP2;2
PvPIP2;3
RcPIP2;1
RsPIP2A
RsPIP2B
RsPIP2C
SoPIP2;1
TgPIP2;1
TgPIP2;2
ZmPIP2;1
ZmPIP2;4
ZmPIP2;5
PIP1 subclass
PIP2 subclass
C
PpPIP1;1
PpPIP1;2
PpPIP1;3
PpPIP2;1
PpPIP2;2
PpPIP2;3
PpPIP2;4
Helix 1
Loop A
Helix 2
Loop B
Helix 3
Loop C
Helix 4
Loop D
Helix 5
Loop E
Helix 6

Fig. S1. Amino acid sequence alignment of plant PIP1 and PIP2 proteins. *A.* Sequence alignment of OsPIPs. Black boxes show the water pore forming residues. The segments for 5 loops and 6 helixes in OsPIPs were indicated. The arrow indicated the Ala/Ile(Val) site difference which was the focus of the current study. *B.* Part of the sequence alignment for plant PIPs with identified activity. Black boxes show the water pore forming residues. The arrow indicated the Ala/Ile(Val) site. Here RsPIP1A, 1B, and 1C correspond to RsPIP1-1, 1-2, and 1-3, and RsPIP2A, 2B, and 2C to RsPIP2-1, 2-2, and 2-3, respectively. *C*. Amino acid sequence alignment of *Physcomitrella patens* PIP1 and PIP2 proteins. The arrow indicated the Ala/Ile(Val) site in *Physcomitrella patens* PIPs The black box and the segment for 5 loops and 6 helixes are the same as in (A).

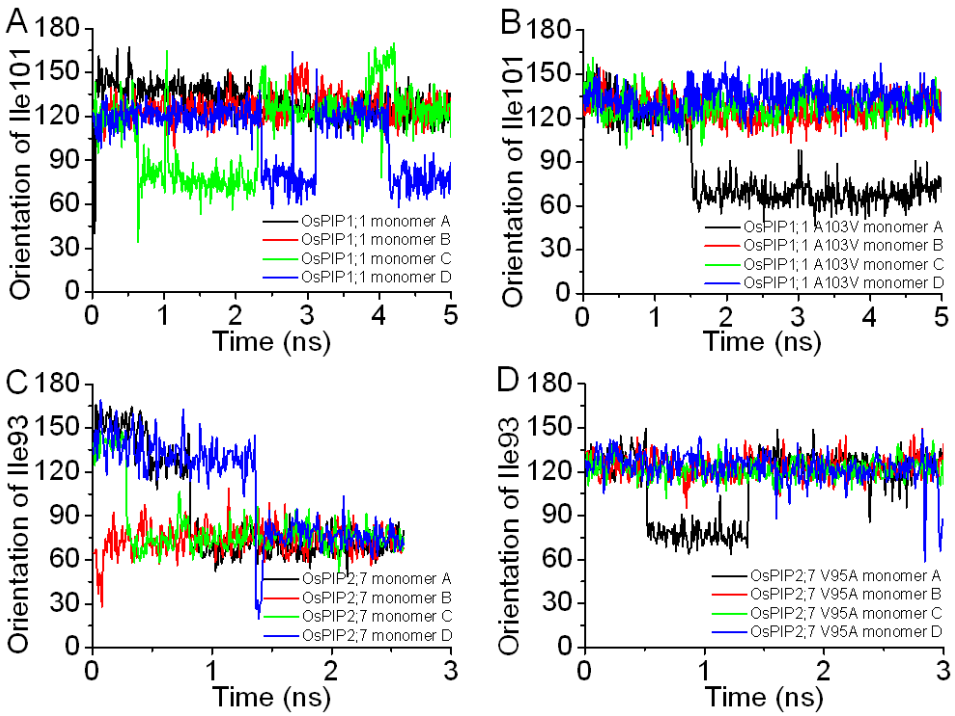

Fig. S2. Orientation evolution of the Ile side chain around NPA. *A & B.* Orientation of Ile101 in OsPIP1;1 (A) and in OsPIP1;1 A103V (B). Ile101 was stable at 127° in OsPIP1;1 A103V as compared to WT. *C & D.* Orientation of Ile93 in OsPIP2;7 (C) and OsPIP2;7 V95A (D). Ile93 in OsPIP2;7 veered to 68° as compared to stable orientation at 127° in OsPIP2;7 V95A. The orientation was denoted by the angle between Ile101/93 (from atom CD to atom CG2 or CD→CG2) vector and *Z*-axis vector (parallel to water channel and pointing from the cytoplasmic to extracellular domain).

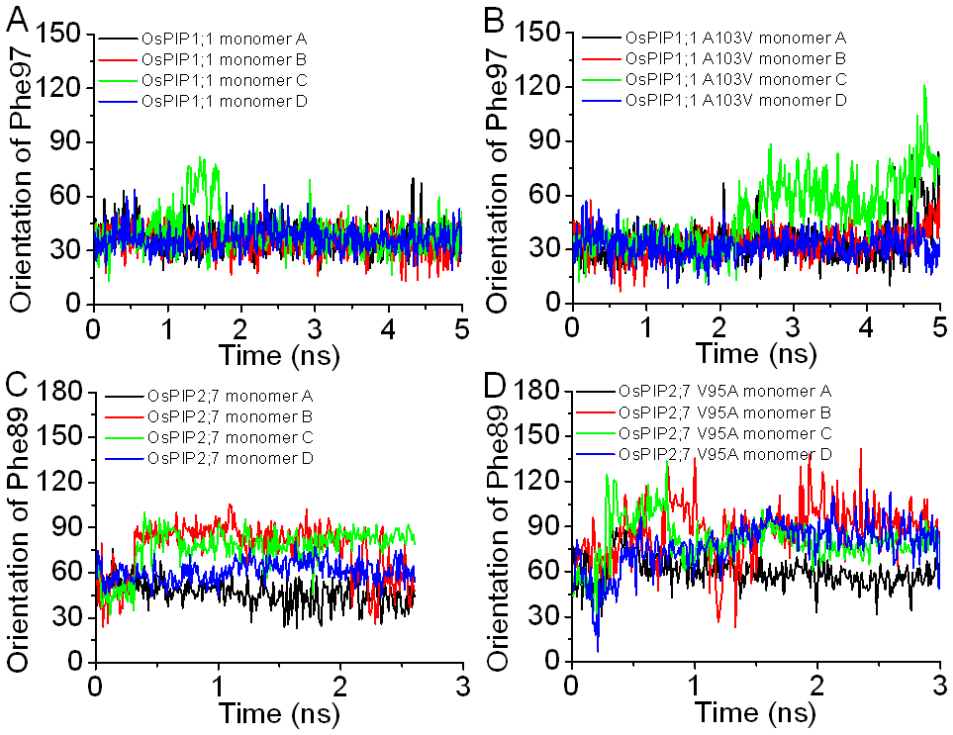

Fig. S3. Orientation evolution of the Phe side chain in ar/R. *A & B.* Orientation of Phe97 in OsPIP1;1 (A) and OsPIP1;1 A103V (B). Phe97 side chain orientation was more stable at ~38° in OsPIP1;1 while it veered to ~38-120° for OsPIP1;1 A103V. *C & D.* Orientation of Phe89 in OsPIP2;7 (C) and OsPIP2;7 V95A (D). Phe89 side chain oriented at 46-88° for OsPIP2;7 and veered to 7-141° for OsPIP2;7 V95A. The orientation was expressed using the angle between Phe97/89 (CD2→CD1) vector and *Z*-axis vector.

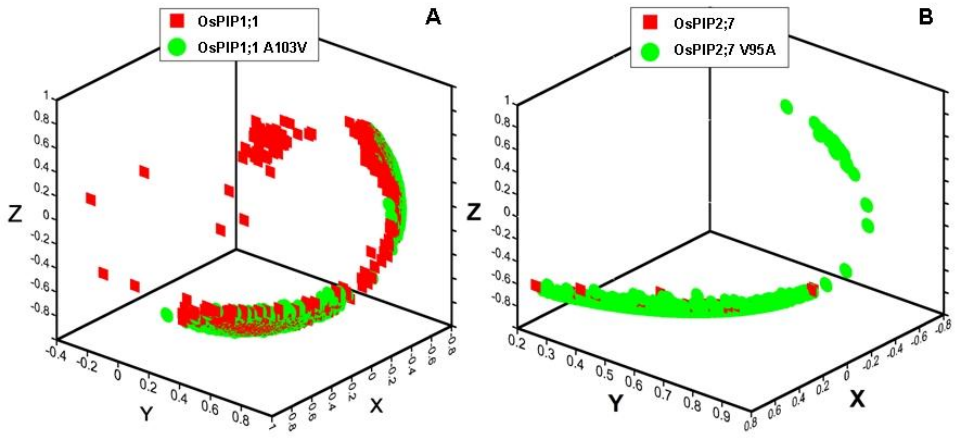

Fig. S4. Motion freedom difference of Phe102 for OsPIP1;1 (A) and of Phe94 for OsPIP2;7 (B). Motion freedom of Phe102/94 was presented as the spatial distribution of its normalized vector CB→CZ during the entire equilibrium process (where one data point was denoted as the vector at one moment in time). Data indicated that the freedom of motion of Phe102 was confined for OsPIP1;1 A103V (*green points*) as compared to that for OsPIP1;1 (*red points*), which induced the enhancement of helix 2 orientation angle (A). High Phe94 freedom of motion was observed in OsPIP2;7 V95A, which countered the impact on helix 2 orientation (B).

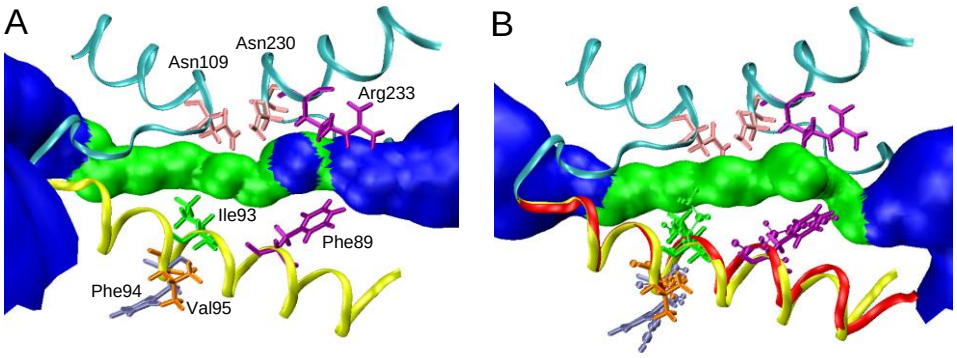

Fig. S5. Structural model for OsPIP2;7 V95A mutation. A typical monomer snapshot was illustrated for OsPIP2;7 alone (A) and for both OsPIP2;7 and OsPIP2;7 V95A at 2.33 *ns* (B). Channel structure was partially represented as a ribbon with the helix 2 (*yellow*), two NPA motifs with the corresponding half-helixes and loops (*cyan*), and channel radius profile. Two Asn from the NPA motif, an Arg from the ar/R region, and the residues (Val95, Phe94, Ile93, Phe89) pertinent to the proposed model were illustrated as licorice in the same color as in Fig. 2*A* and 3*B*. OsPIP2;7 V95A mutation drove an helix 2 orientation change (*yellow* for WT and *red* for V95A), which induced unstable and unfavorable orientations of Ile93 residue at the NPA region and of Phe89 residue at the ar/R region (*CPK* presentation). Such orientation change reduced the channel pore, narrowed the radius profile, and, combined with a poorly-formed water molecule file, reduced the water permeability.

Plant Biology:

Identification of a Residue in Helix 2 of Rice Plasma Membrane Intrinsic Proteins That Influences Water Permeability

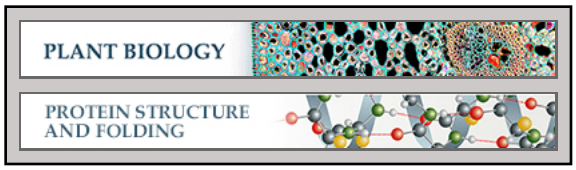

Minhua Zhang, Shouqin Lü, Guowei Li, Zhilei Mao, Xin Yu, Weining Sun, Zhangcheng Tang, Mian Long and Weiai Su

J. Biol. Chem. 2010, 285:41982-41992.
doi: 10.1074/jbc.M110.101790 originally published online October 6, 2010